

Received 9 November 2023, accepted 15 December 2023, date of publication 19 December 2023,
date of current version 29 December 2023.

Digital Object Identifier 10.1109/ACCESS.2023.3345248

RESEARCH ARTICLE

Raytracing Digital Foliage at Millimeter-Wave: A Case Study on Calibration Against 60-GHz Channel Measurements on Summer and Winter Trees

CHIEHPING LAI¹, DAMIR SENIC², CAMILLO GENTILE¹, (Member, IEEE), JELENA SENIC^{3,4},
AND NADA GOLMIE⁵

¹Radio Access and Propagation Metrology Group, National Institute of Standards and Technology (NIST), Gaithersburg, MD 20899, USA

²Ansys Inc., Canonsburg, PA 15317, USA

³Associate, Radio Access and Propagation Metrology Group, National Institute of Standards and Technology, Gaithersburg, MD 20899 USA

⁴Department of Physics, University of Colorado, Boulder, CO 80309, USA

⁵Communications Technology Laboratory, National Institute of Standards and Technology (NIST), Gaithersburg, MD 20899, USA

Corresponding author: Camillo Gentile (camillo.gentile@nist.gov)

ABSTRACT Accurate channel propagation modeling of foliage is critical to the design of wireless networks, given its pervasive nature in rural, suburban, and urban environments. Its blockage effects can be particularly devastating at millimeter-wave (mmWave) because the size of leaves and branches is comparable to the wavelength of the transmitted signal. While raytracing models are firmly based on electromagnetic principles, reliability can be attained only through calibration against measurements. In the few works that do so, foliage is represented as simple canonical shapes (cylinders, discs, etc.) and calibration is performed against measurements with foliage integrated as part of entire outdoor environments. The controlled approach that we adopt in this paper, rather, is based on measurement of single specimens of foliage, for precision characterization. To sustain this precision at mmWave, the foliage is represented digitally as a mesh of faceted leaves and branches. Raytracing predictions from the Ansys HFSS SBR+ model applied to digital twins of seven trees are calibrated against measurements—collected in summer and in winter for comprehensive analysis—with the Terragraph double-directional 60-GHz channel sounder. The tree-specific predictions, which can then be integrated as part of an entire outdoor environment, are shown to match the measurements very well.

INDEX TERMS 5G, mmWave, foliage, penetration loss, propagation, Ansys HFSS SBR+, raytracing, tuning, Terragraph, vegetation, wireless networks.

I. INTRODUCTION

By exploiting swaths of available spectrum, millimeter-wave (mmWave) communications will play a key role in increasing the throughput and capacity of 5G networks. The 60 GHz band – precisely 57 GHz to 71 GHz – is particularly appealing, as much due to its ultrawide bandwidth as to its unlicensed usage. The *IEEE 802.11ay* standard for next-generation WiFi, which operates in this band, can deliver up to 20 Gigabits/s data rate; it was certified recently, in July

The associate editor coordinating the review of this manuscript and approving it for publication was Chakchai So-In.

2021 [1]. While there is strong impetus from international consortia such as the *Telecom Infra Project* [2] for large-scale deployment of *IEEE 802.11ay* (and *IEEE 802.11ad*, an earlier version) for backhaul and urban public access outdoors, deployment has been stifled by concerns about propagation loss at 60 GHz [3]. Although free-space propagation itself is not frequency dependent [4], oxygen-absorption loss and penetration loss from typical outdoor obstructions – such as buildings, vehicles, and foliage – can be significant [5].

Of particular concern at 60 GHz is penetration loss due to foliage because the size of leaves and branches is comparable

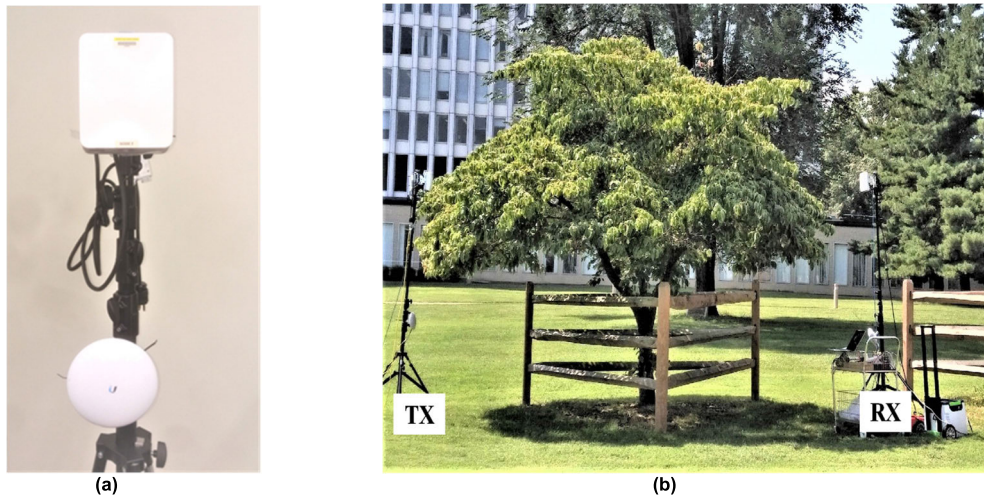


FIGURE 1. Terragraph transceiver. (a) The rectangular radome (upper part) houses an 8×36 planar phased-array antenna that operates at 60 GHz. The parabolic WiFi antenna (lower part) operates at 5 GHz and is used for synchronizing the double-directional electronic beam scans between the transmitter and receiver. (b) Terragraph channel sounder during the summer measurement campaign. The transmitter and receiver antennas were placed at the same height with the arrays facing each other.

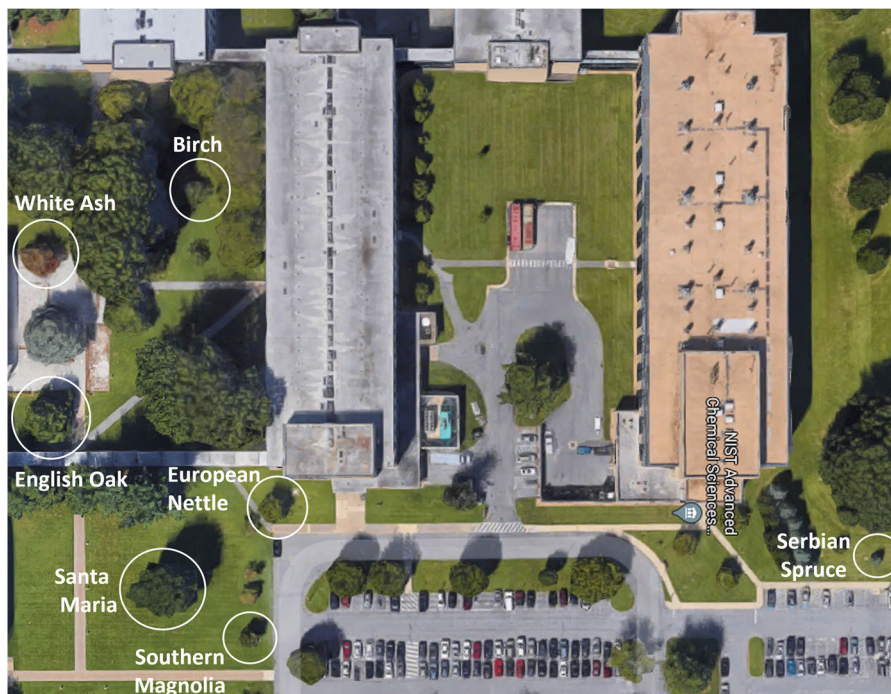


FIGURE 2. Bird's-eye view of the NIST campus in Gaithersburg, Maryland, showing the seven trees that were measured in the study.

to the 5 mm wavelength of the transmitted signal, and so they appear electrically large. Indeed, individual trees can inflict loss up to 40 dB on the signal, as we shall see later. Trees are important to consider in network design as they are *pervasive* – in all outdoor environments, rural, suburban, and urban alike – and *intrusive* – often tall and so obstruct even high cell towers, rooftop backhaul links, or deployment on lampposts for public urban access. And because trees cluster

naturally in forest, parks, etc., the large penetration loss of individual trees is intensified by a factor of 100 (20 dB), 1000 (30 dB), or even more, potentially limiting service. What is needed for proper design and deployment of large-scale networks is an accurate channel propagation model of the environment, including foliage. Previous work on channel propagation modeling of foliage loss can be categorized into empirical and theoretical models.

Empirical models are fit directly to measurements, with typical model parameters being center frequency, tree type, number of trees, and season. Numerous measurement campaigns have been conducted thus far to support these models [6], [7], [8], [9], [10], [11], [12], [13], [14], [15], [16], [17]: In [6], foliage loss through a single tree was measured, and in [7], [8], [9], [10], [11], and [12] through multiple trees. Loss for coniferous and leaved/leafless deciduous trees at 2 GHz, 5 GHz, 29 GHz, and 60 GHz and for various wind speeds was characterized in [13]; in [14], these measurements were used to develop a model for signal fading of a swaying tree. In [7], loss was computed as a function of number of trees and compared between leaved and leafless cases. In [15], the received signal at 33 GHz was compared in urban environment, in the presence and absence of leaves and in the absence of trees altogether. In [16], loss at 28 GHz was compared between spring and fall. Besides loss, a few studies reported the effects of foliage on channel parameters such as root mean square (RMS) delay and angular distributions, mean excess delay, coherence bandwidth, and number of propagation paths to the receiver [11], [15], [17]. Theoretical models, on the other hand, predict foliage loss based on electromagnetic principles [18], [19]: A dynamic raytracing-based channel model for trees in an urban environment at 28 GHz was analyzed in [18]. Another study compared a power map – also generated from raytracing – in the presence of foliage at 2 GHz and 60 GHz, emphasizing the need for geographical maps to integrate detailed vegetation [19].

A few hybrid approaches that combine both empirical and theoretical models have appeared recently, in which raytracing models were calibrated against mmWave measurements. In [20], [21], [22], and [23], foliage was integrated as part of the entire outdoor environment: In [20], foliage was shaped as a dielectric slab containing randomly oriented leaves (discs) and branches (cylinders) and raytracing predictions for foliage loss, delay spread, and angular spread were calibrated against 28 GHz measurements collected in an urban canyon street; in [21] and [22], the tree canopies and trunks were shaped as rectangularoids and the measurements were collected in a parking lot at 28 GHz; in [23], trees were shaped as right and concentric cylinders and measurements were collected in three dense-scatter urban environments at 28 GHz and 73 GHz. A different approach was taken in [24], in which small indoor plants were isolated from their natural habitat and characterized in a controlled manner: predictions from raytracing their canopies shaped as point scatterers were calibrated against 18 GHz and 60 GHz measurements of 12 single specimens placed on a rotator in an anechoic chamber.

The hybrid approach proposed in this paper most closely resembles [24], in which a raytracing model is calibrated against 60 GHz channel measurements of single specimens. We maintain that this controlled approach renders more realistic predictions, which not only translate to enhanced accuracy when integrated as part of an entire outdoor environment,

but are also more generalizable to different shapes and deployments (number and placement of trees) through the environment. How our approach differs from [24] is that we consider outdoor trees instead of indoor plants and because the trees are large – up to 12 m in diameter – the trees had to be measured in their natural habitat. Another significant difference from [24] – and in fact from all aforementioned empirical, theoretical, and hybrid models – is that rather than simplifying the tree models into canonical shapes such as discs, cylinders, and rectangularoids, we are the first to consider digital foliage, that is, a mesh of ten thousands of miniature facets that constitute the leaves and branches; this is critical at mmWave since their size is comparable to the signal wavelength. While such a detailed approach may have been prohibitive in the past, recent development of Graphics Processing Unit (GPU)-based raytracing can predict an environment with millions of triangles in just seconds [25], [26], [27], [28].

The main contributions of this paper are as follows:

1. Channel measurements with the *Terragraph*¹ [29] 60 GHz phased-array channel sounder that estimates path loss (PL), angle-of-departure (AoD), and angle-of-arrival (AoA) per double-directional scan of electronic beams;
2. An extensive measurement campaign on seven trees – during summer and winter to compare seasonal effects – comprising 14 different TX-RX locations per tree and 4096 channel scans per location, for a total of 573440 scans;
3. Calibration of *Ansys HFSS SBR+* (High Frequency Structure Simulator Shoot and Bouncing Ray) raytracing model¹ [30] applied to digital twins of the seven trees against the measurements.

The remainder of the paper is developed as follows: in Section II, we describe the *Terragraph* channel sounder and the measurement campaign; Section III describes the *Ansys HFSS SBR+* raytracing model, including the digital trees and the methodology for calibrating the raytracing predictions against the measurements. Section IV reports a comparison of the measured and predicted results, as well as the lessons learned from the calibration process; the last section is reserved for conclusions.

II. CHANNEL SOUNDER AND MEASUREMENT CAMPAIGN

This section describes the *Terragraph* channel sounder and the measurement campaign it was used to conduct.

A. TERRAGRAPH CHANNEL SOUNDER

Terragraph transceivers were used as both the transmitter (TX) and receiver (RX) ends of the channel sounder.

¹Certain equipment, instruments, software, or materials, commercial or non-commercial, are identified in this paper in order to specify the experimental procedure adequately. Such identification is not intended to imply recommendation or endorsement of any product or service by NIST, nor is it intended to imply that the materials or equipment identified are necessarily the best available for the purpose.

TABLE 1. The seven trees measured in summer and in winter.

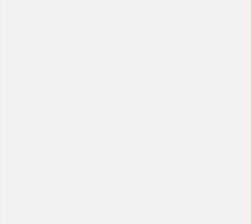
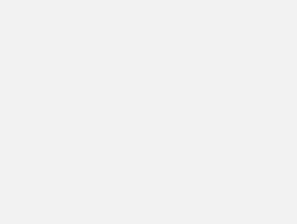
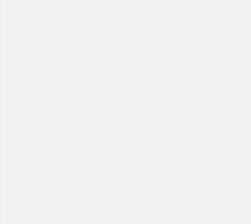
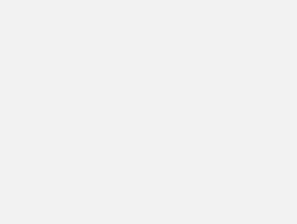
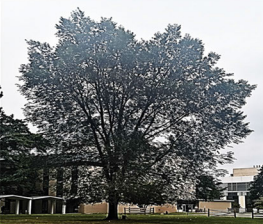
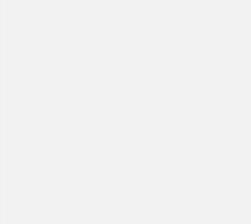
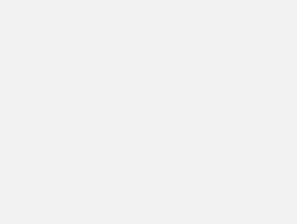
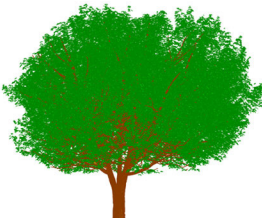
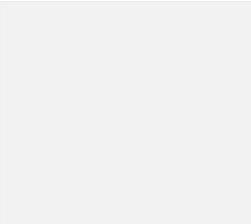
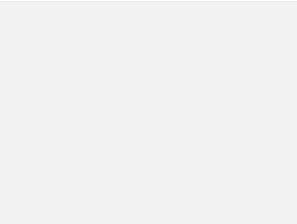
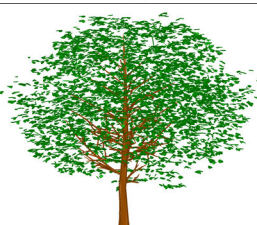
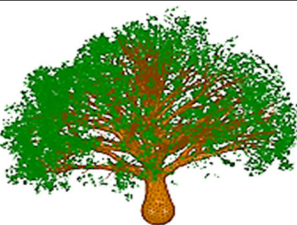
Tree	Summer Trees		Winter Trees	
	Photograph	Digital tree	Photograph	Digital tree
Serbian Spruce				
Southern Magnolia				
Santa Maria				
White Ash				
European Nettle				
Birch				
English Oak				

TABLE 2. Physical properties and channel statistics of the ten measured trees.

Tree type		Physical properties					Channel statistics					KS stat.
		Diameter, meas. = model (m)	Height, meas. (m)	Leaf density, model (facets/m ³)	Branch density, model (facets/m ³)	Leaf + branch density, model (facets/m ³)	Total penetr. loss mean (dB)	Total penetr. loss std. dev. (dB)	RMS angle mean (deg.)	RMS angle std. dev. (deg.)		
Summer	Serbian Spruce	5	7.5	466	11	477	Meas.	35.0	3.9	6.8	3.4	0.14
	Model						35.0	4.5	7.1	3.2		
	Southern Magnolia	5	5.2	92	5	97	Meas.	28.1	5.5	6.9	3.0	0.16
							Model	27.6	4.1	6.3	3.4	
	Santa Maria	6	17.4	91	4	95	Meas.	28.6	5.0	7.4	4.0	0.14
							Model	28.6	5.1	7.6	2.9	
	White Ash	8	6.3	75	5	80	Meas.	24.3	6.7	6.9	3.6	0.15
Model							24.6	5.7	6.7	3.0		
European Nettle	4.5	6.0	83	14	97	Meas.	27.0	4.4	7.8	3.4	0.15	
						Model	28.0	5.3	7.0	4.1		
Birch	5.5	6.3	89	9	98	Meas.	27.5	4.6	6.7	3.2	0.12	
						Model	28.1	5.7	6.4	3.0		
English Oak	12	16.2	143	45	188	Meas.	27.4	2.1	7.5	3.4	0.16	
						Model	27.4	2.1	5.9	3.1		
Winter	European Nettle	4.5	6.0	25	14	39	Meas.	22.2	4.5	7.3	3.3	0.17
							Model	22.3	5.2	7.4	4.1	
	Birch	5.5	6.3	31	9	40	Meas.	23.8	6.6	7.7	3.3	0.13
Model							23.3	6.5	7.6	2.8		
English Oak	12	16.2	50	45	95	Meas.	26.1	5.1	7.1	3.5	0.18	
						Model	25.9	4.9	5.5	3.8		
All Summer		6.6	9.3	148.2	13.3	161.5	Meas.	29.6	4.8	7.2	3.5	0.07
Model							29.7	4.8	6.7	3.3		
All Winter		7.3	9.5	35.3	22.7	58.0	Meas.	24.3	5.5	7.4	3.4	0.18
Model							24.1	5.6	6.8	3.6		
All		6.8	9.3	114.3	16.1	130.4	Meas.	28.6	5.0	7.2	3.4	0.06
Model							28.7	5.0	6.8	3.3		

See Fig. 1. The transceiver features an 8 × 36 planar phased-array antenna with 2.5 mm spacing between elements, corresponding to half-wavelength spacing at the 60 GHz center frequency of the system. The antenna synthesizes a vertically polarized beam with 2.8° beamwidth in azimuth and 12° in elevation that is electronically scannable. Since only the 36 columns are phased, the beam is scannable in azimuth alone, from -45° to 45° at 1.4° steps, for a total of 64 single-directional scans at one end, or equivalently 64 × 64 double-directional scans at both ends. The system reports path loss directly, meaning that it already de-embeds the TX power and the TX and RX beam gains from the RX power measured. Given the 16 dBm TX power and the 29 dBi beam gain, the maximum measurable pathloss of the system is 136 dB. Note that when the RX power falls below the noise floor, no pathloss value is reported. When reported, the scanned path loss is indexed by the boresight angle-of-departure (AoD) of the TX beam and the boresight angle-of-arrival (AoA) of the RX beam. The AoD and AoA are reported with respect to the normal of the phased-array antenna board (AoD=AoA=0°).

B. MEASUREMENT CAMPAIGN

Measurements were collected on the National Institute of Standards and Technology (NIST) campus in Gaithersburg, Maryland. To explore the seasonal effects of propagation through trees, one measurement campaign was conducted in summer on seven different trees – Serbian Spruce, Southern Magnolia, Santa Maria, White Ash, European Nettle, Birch, and English Oak – followed by another campaign in winter on a subset of the three deciduous trees – European Nettle, Birch, and English Oak – after the leaves had withered. Fig. 2 shows a bird’s-eye view of the NIST campus and the seven trees that were measured, and photographs of the trees appear in Table 1. The diameter of their canopy ranged between 4.5 m to 12 m over all trees, with exact values compiled in Table 2.

The TX and RX antennas were positioned at the same height (4.6 m) and placed about 1 m from the canopy, with the antennas pointed towards each other (their normals aligned), as shown in Fig. 1(b). The height was high enough for the elevation beamwidth of the antennas to fall completely within the canopy of all trees. To observe the path loss through different cross sections of the tree, the RX was moved to 14 distinct

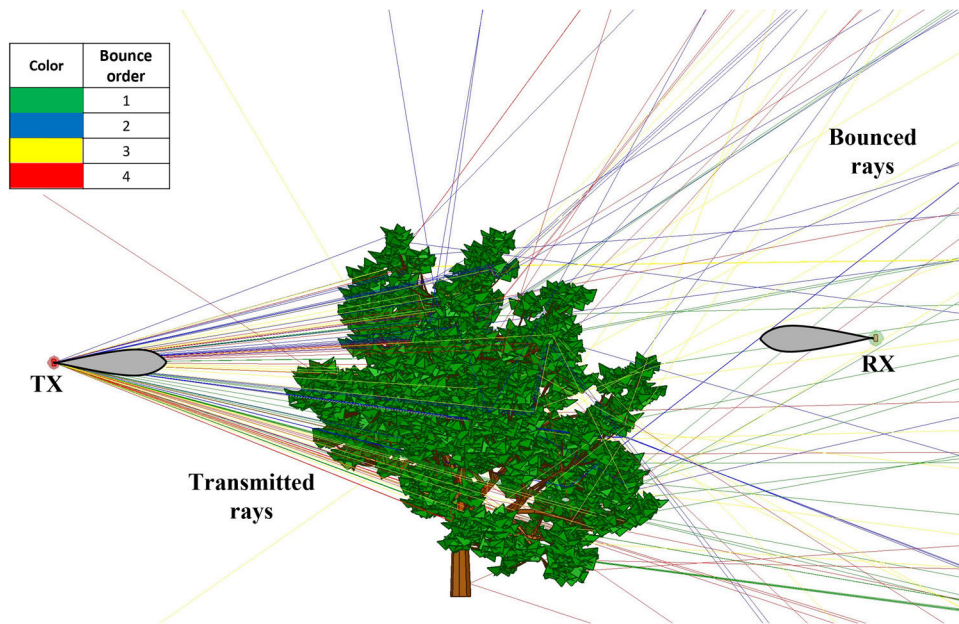


FIGURE 3. Illustration of a double-directional electronic beam scan raytraced with Ansys HFSS SBR+ on the digital European Nettle tree. The rays are emitted from the TX antenna and reflected and diffracted from the tree leaves, branches, and trunk, impinging on the RX antenna. The beam patterns of the TX and RX are shown, and the rays are color-coded in the legend against the number of bounces. (The number of rays in the illustration was reduced by a factor of 60 to improve visualization.)

locations around each tree while the TX was maintained fixed at a single location. The TX-RX distance was recorded at each RX location so that the path loss reported could be converted into foliage loss, by subtracting the free-space loss given by the distance through Friis transmission equation [31]. Thus the foliage loss represents the excess loss in propagating through the tree vis-à-vis no tree at all.

III. RAYTRACING MODEL AND CALIBRATION

This section describes the Ansys HFSS SBR+ raytracing model and the digital trees on which it was applied to predict foliage loss, as well as how the digital trees were calibrated against the measurements.

A. ANSYS HFSS SBR+ RAYTRACING MODEL

The Ansys HFSS SBR+ raytracing model is an asymptotic high-frequency electromagnetic simulator for modeling interactions in electrically large environments, that is, when the wavelength is smaller or comparable in size to the objects simulated; in this case, the electromagnetic waves can be approximated by rays. At 60 GHz, the wavelength is 5 mm and the smallest object simulated is 41 mm² (a leaf on the Serbian Spruce). The simulator employs the shooting and bouncing ray (SBR) technique for the rapid computation. SBR+ extends the (basic) SBR technique by overlaying advanced diffraction physics such as the physical theory of diffraction (PTD), the uniform theory of diffraction (UTD), and creeping wave physics for high-fidelity scattering in shadowed regions. All these propagation mechanisms enhance the model fidelity, precisely accounting for critical large-scale

interaction effects, including diffraction, blockage, and multi-bounce, which are crucial to obtain realistic predictions when a mmWave signal encounters foliage obstacles.

In SBR+, the PTD and UTD account for the additional propagation mechanisms neglected in SBR due to truncation of uniform Physical Optics (PO) currents at sharp angular discontinuities (“wedges”) and blockage of SBR’s Geometrical Optics (GO) rays: PTD is simply a numerical correction to the scattered fields radiated by PO currents near wedges, whereas UTD launches bundles of edge-diffraction rays from directly illuminated portions of each wedge along the Keller cone; once transmitted, the UTD rays behave exactly like SBR rays, propagating according to GO and painting PO currents at each bounce, modeled as specular reflections, that contribute to the scattered field. The UTD rays often illuminate portions of the SBR scattering geometry that are never reached by SBR GO rays transmitted directly from the field source. Creeping wave physics are only applicable to curved metallic surfaces and thus were not considered in this study.

The coupling between the TX and RX antennas is modeled as simulated beams at both ends, whose azimuth and elevation gain patterns are matched to the beam synthesized by the Terragraph channel sounder. In the simulations, the double-directional beam is scanned in the same progression as in the measurements, for unbiased comparison. All rays were shot from the TX antenna’s phase center with the ray density parameter set to four rays per wavelength and the maximum number of bounces set to five. Fig. 3 shows an illustrative example of the transmitted and bounced rays for one scan on the European Nettle tree. The radiation

TABLE 3. Distribution of received rays per RX location.

		Total rays transmitted (#)	1 st -order bounces received (# / % of total transmitted)	2 nd -order bounces received (# / % of total transmitted)	3 rd -order bounces received (# / % of total transmitted)	4 th -order bounces received (# / % of total transmitted)	Power ratio of LoS ray to all received rays (%)
Summer	Serbian Spruce	8828628	251751 / 2.9	94709 / 1.1	104720 / 1.2	63583 / 0.7	0
	Southern Magnolia	13031115	487419 / 3.7	282173 / 2.2	199249 / 1.5	140941 / 1.1	0
	Santa Maria	17444916	323470 / 1.9	148733 / 0.9	89401 / 0.5	60526 / 0.3	0
	White Ash	9773441	1170215 / 12.0	756990 / 7.7	502757 / 5.1	360096 / 3.7	0
	European Nettle	11420440	222064 / 1.9	177094 / 1.6	178917 / 1.6	160439 / 1.4	0
	Birch	11957243	1973024 / 16.5	781304 / 6.5	392757 / 3.3	219238 / 1.8	0
	English Oak	15769666	905686 / 5.7	433341 / 2.7	244969 / 1.6	146880 / 0.9	0
Winter	European Nettle	832606	392336 / 47.1	72906 / 8.8	17698 / 2.1	5599 / 0.7	6.8
	Birch	9793371	947648 / 9.7	395735 / 4.0	238844 / 2.4	152586 / 1.6	4.1
	English Oak	6106788	1050645 / 17.2	365253 / 5.9	153174 / 2.5	64999 / 1.1	2.3
All Summer		12603635	761947 / 6.4	382049 / 3.2	244681 / 2.1	164529 / 1.4	0
All Winter		5577588	796876 / 24.7	277964 / 6.2	136572 / 2.4	74394 / 1.1	4.4
All		10495821	772425 / 11.9	350823 / 4.1	212248 / 2.2	137488 / 1.3	1.3

patterns of the TX and RX beams are shown and the rays are color-coded against the number of bounces. Table 3 provides a distribution of the bounce order of the rays per RX location as well as the power ratio of the line-of-sight (LoS) ray to the total power of the received rays. Note that the LoS ray is always blocked for the summer trees.

The RX power per scan was computed by summing over the power of all rays impinging on the RX antenna. The RX sensitivity was set to that of the Terragraph channel sounder, and so in kind was not reported if it fell below the noise floor. The RX power was then converted to path loss by subtracting the TX power and the double-directional boresight gains of the TX and RX beams, as was done in the measurements. Likewise, the path loss was then converted to foliage loss per RX location through Friis transmission equation given the TX-RX distance.

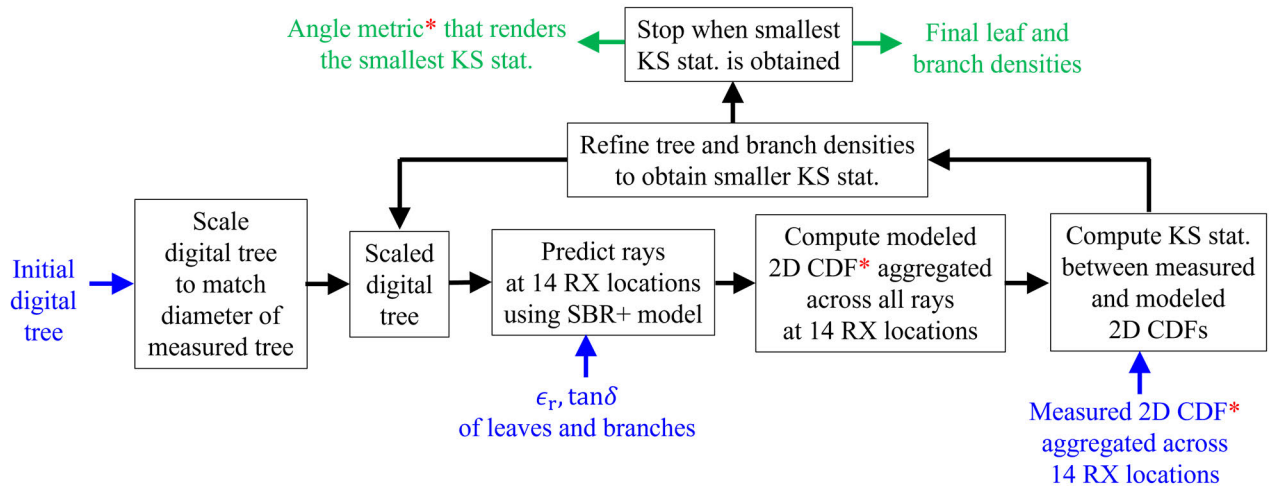
B. DIGITAL TREES AND CALIBRATION

The trees were represented in HFSS SBR+ as digital CAD databases, each defined as a 3D faceted mesh. Hundreds of commercially available databases were inspected beforehand to select the seven most similar to the trees measured. Once selected, the digital trees were scaled to the dimensions of

their live counterparts. Then the mesh facets were partitioned into two classes – leaves and branches/trunk – and assigned distinct electrical properties. Namely, for all trees, the leaves were assigned relative permittivity $\epsilon_r = 1.5$ and electric loss tangent $\tan\delta = 0.33$ [32], [33], [34], while the branches/trunk were assigned $\epsilon_r = 55$ and $\tan\delta = 0.218$ [33], [35], [36]. The digital models appear side-by-side with the photographs in Table 1 for summer and for winter. For winter, only the deciduous European Nettle, Birch, and English Oak were considered; the Serbian Spruce, Southern Magnolia, Santa Maria, and White Ash² are coniferous and so were not considered.

Commercially available digital trees are typically generated automatically through graphical design software from photos, videos, lidar, etc. for manufacturing purposes. As a result, they often contain physical details much smaller than the 5 mm wavelength of our channel sounder, thus are irrelevant to electromagnetic simulations; moreover, their sheer size triggered extensive mesh creation in the simulation, causing it to fail. Therefore, it was necessary to prune the

²Although the White Ash is actually classified as deciduous, the leaf density withered less than 50 % in winter and so was not considered for winter.



*Five separate angle metrics were considered to generate the 2D CDF: $|\text{AoD}|$, $|\text{AoA}|$, $|\text{AoD}+|\text{AoA}|$, $|\text{AoD}-\text{AoA}|$, $|\text{AoD}+|\text{AoA}+|\text{AoD}-\text{AoA}|$

FIGURE 4. Flowchart of the process to calibrate the digital trees against the measurements. The inputs to the process are the initial digital tree, the electrical properties of its leaves and branches, and the measured 2D CDF. The outputs are the final leaf and branch densities as well as the angle metric that renders the smallest KS static, which was found to be $|\text{AoD}| + |\text{AoA}|$.

databases to a computationally manageable size in preprocessing. This was accomplished with *Ansys SpaceClaim*¹, reducing the initial size by up to 70 % depending on the CAD model vendor and the tree density, by deleting the tiniest leaves and branches and smoothing the intricacies of the branches and the trunk. *SpaceClaim* was also used to trim the leaf density when generating the winter version of the trees. Once the models were preprocessed, the leaf and branch densities were adjusted further through precision calibration – by either increasing or decreasing them – in order to obtain the best match of the predictions to the measurements, as described in the next section. For winter, this often meant adding branches that were not in the commercial database. A flowchart of the calibration process is shown in Fig. 4. The digital trees shown in Table 1 correspond to the final leaf and branch densities, which are outputs of the calibration process. The densities are reported for each tree in Table 2.

IV. RESULTS

In this section, we compare the channel properties of the seven trees in summer and in winter between the measurements described in Section II and the raytracing model described in Section III: the measurements are discussed in the first subsection and the model in the second subsection.

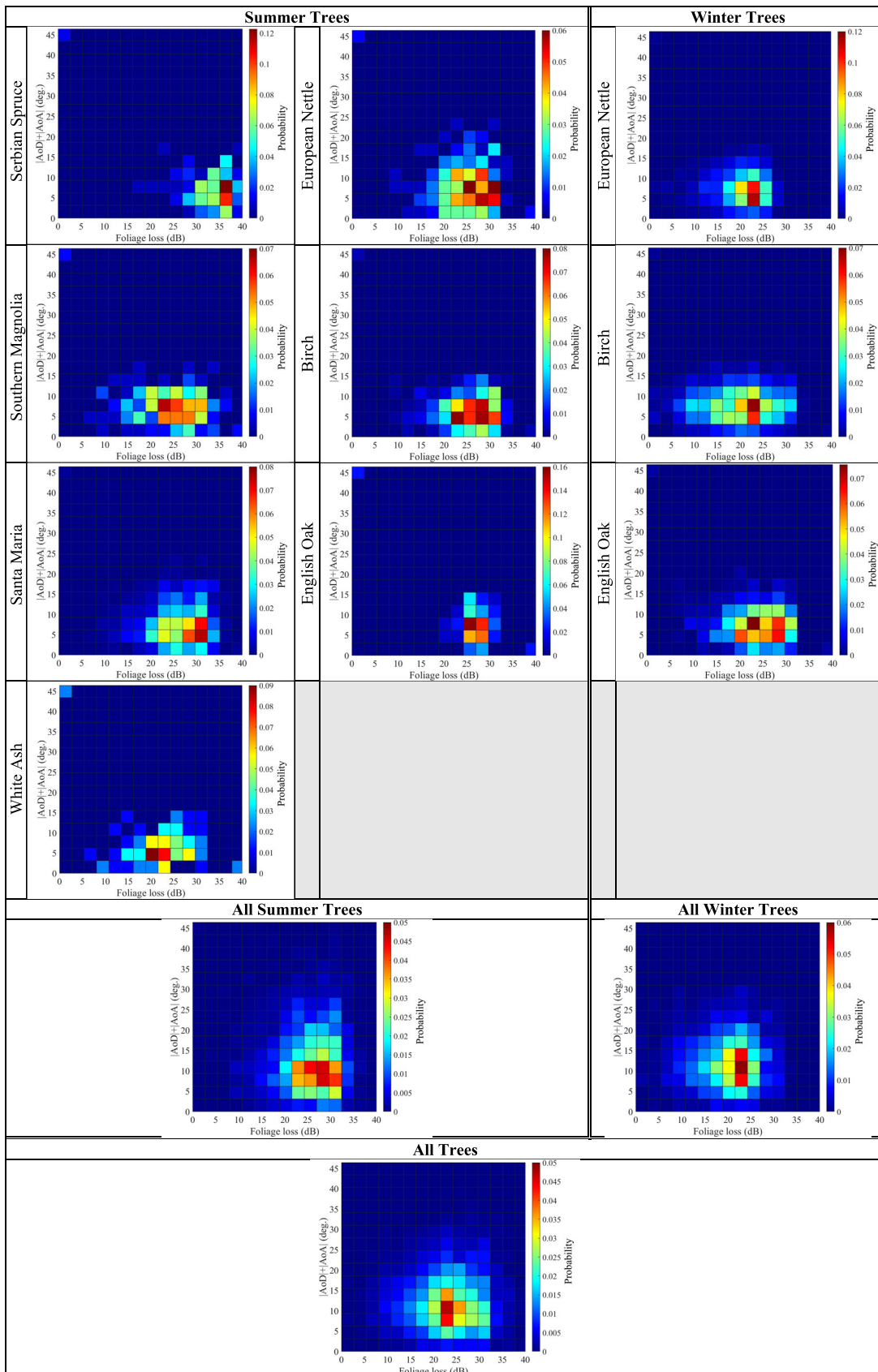
A. MEASUREMENT

The total foliage loss inflicted by the tree is equivalent to the loss an omnidirectional RX antenna would detect from an omnidirectional TX, and so is an important reference metric. It is computed from our measurements by summing over the foliage loss from the 4096 double-directional scans per RX location. To compare the metric between trees, the mean (and standard deviation) of the total foliage loss per tree is reported in Table 2, averaged over all 14 RX locations per tree. Also

reported at the bottom of the table are the statistics averaged over all summer trees, averaged over all winter trees, and averaged over all trees. The foliage loss decreased in winter versus summer due to the decreased leaf density (the branch density was kept constant), on average by 5.3 dB; the smallest decrease was observed for the English Oak, both because the leaf density was still relatively high (compared to the other two deciduous trees, European Nettle and Birch) and because the branch density was the highest. In fact, the combined leaf + branch density was found to be an excellent predictor of the average penetration loss across all trees, in that the Pearson correlation coefficient between the two is exactly 1.0 – the maximum obtainable – meaning that the lower the density, the lower the foliage loss.

The angular distribution of the foliage loss is also an important metric – in particular for 5G systems since they are highly directional – to represent the equivalent loss that a directional RX antenna would detect from a directional TX. Given the double-directionality of the channel sounder, the angle is computed as $|\text{AoD}| + |\text{AoA}|$, which represents the double-directional angular displacement from boresight, which we found to more accurately model the angular distribution – as we shall see in the next subsection – than the separate single-directional angles, (AoD, AoA), reported by the system. The RMS mean of the angle (weighted by the foliage loss) is reported for all trees in Table 2 and was found to vary little – only from 6.7° to 7.7° – across the trees. The RMS standard deviation of the angle was also found to vary little – only from 3.0° to 4.0° – across all trees. Although the statistics for the total foliage loss and for its angular distribution reported in Table 2 are useful references for comparison to literature, the statistics are quantified separately in the two domains; in reality, the total foliage loss and its angular distribution are dependent. To observe this

TABLE 4. Measurement probability density functions (PDFs).



dependence, we compute the 2D probability density function (PDF) over the two domains per tree, specifically we compute the histogram of the foliage loss versus angle compiled over all scans from the 14 RX locations. They are shown in Table 4 per tree, as are the PDFs further aggregated over all summer trees, all winter trees, and all trees: dark red is the highest probability and dark blue the lowest.

All PDFs exhibit the same trend to varying degrees, although it can be most clearly observed in the PDF for all trees: When the RX is located directly across the TX, bisecting the tree: at $|\text{AoD}| + |\text{AoA}| = 0^\circ$, the double-directional beam is scanned towards the center of the tree – where the leaf and branch densities are thickest and where the trunk can be found – hence large foliage loss is expected. As the beam is scanned away from the center, the densities subside and there are many possible interactions with the canopy (reflection and diffraction) to bend rays emanating from the TX back to the RX, so foliage loss begins to decrease with angle. However, as the beam approaches the edge of the tree, not only does the path length increase, but there are fewer possible rays, so foliage loss then increases with angle. As such, the RMS mean of the angle – the “sweet spot” – is 7.2° for all trees, as reported in Table 2. Note that for the other 13 cases when the RX is not located directly across the TX, the RMS mean of the angle is biased either positively or negatively from the illustrative case, but the symmetry of the 13 locations around the tree effectively cancels the bias.

Although, as stated earlier, the RMS standard deviation of the angle only ranges from 3.0° to 4.0° , the angular distribution of the foliage loss can actually vary quite a bit from tree to tree, as is apparent in Table 4. When comparing summer trees, the combined leaf and branch density appears to be a good indicator of the distribution, where a lower density allows for the foliage loss to spread out wider in angle. This is particularly evident when comparing the White Ash and Southern Magnolia – both have lower summer combined density of 80 facets/m^3 and 97 facets/m^3 respectively and are spread out – to the English Oak and Serbian Spruce – both have higher summer combined density 188 facets/m^3 and 477 facets/m^3 respectively and are concentrated – yet the Birch also has lower density (98 facets/m^3) but its distribution is more comparable to the latter two. This trend of wider spread with lower density also appears to also hold true when comparing the three deciduous trees between summer and winter, in that the distributions of the Birch and the English Oak – winter combined density 40 facets/m^3 and 95 facets/m^3 respectively – are spread out more in winter than in summer, yet this is clearly not the case for the European Nettle (summer combined density 97 facets/m^3 , winter combined density 39 facets/m^3). This may seem surprising since the European Nettle both experiences the greatest percentage drop in density between the two seasons and is by far the tree with the largest diameter. The observed unpredictability in the PDFs from the physical properties of the trees (diameter, leaf and branch densities) underscores the need for a precise

model for prediction. Indeed, in the next section we show how the HFSS SBR+ model predicts the PDFs in Table 4 well.

B. MODEL

As described in Section III-B, the model predictions were set up to mimic the output from the measurements. Specifically, the foliage loss for the 4096 scans per RX location was predicted from the model, from which we compiled statistics analogous to the measurement statistics in Table 2. Based on the mean and standard deviation of the total foliage loss and the mean and standard deviation of the RMS angle, we can see that the model predictions match the measurements very well. Yet, as explained earlier, these statistics are computed over the two domains separately and so do not capture the interdependency between foliage loss and angle that is captured by the PDFs.

To that end, we compared the measurement PDFs to the model PDFs through the two-sample Kolmogorov-Smirnov (KS) test as follows: First, the 2D cumulative distribution function (CDF) was compiled over all scans from the 14 RX locations per tree, separately for the measurement and for the model. The resultant CDFs are shown in Table 5. Once compiled, the KS statistic – the maximum absolute difference between the measurement CDF and model CDF over the two domains – was computed as a goodness-of-fit metric between the two CDFs. The KS statistic can range between 0 (perfect fit) and 1 (worst fit), where 0.16 indicates that the two fit at 95 % confidence level based on the size of the sample sets [37], [38]. The KS statistic is also reported for the seven trees in winter and in summer in Table 2, and ranges from 0.06 to 0.18, indicating good fits between the measurements and the model.

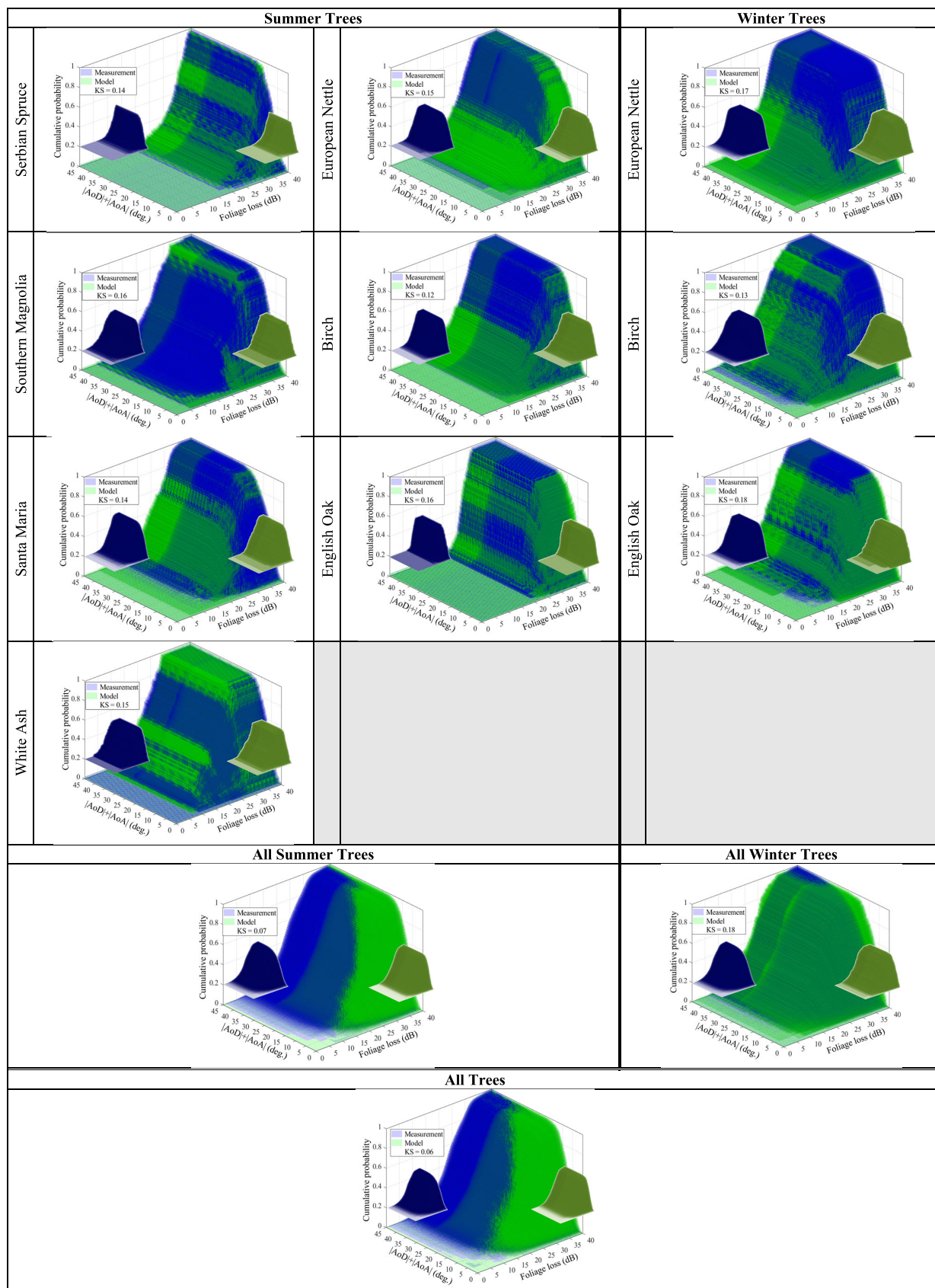
As mentioned in the previous subsection, the angle metric used to compute the 2D PDFs (and 2D CDFs) was selected as $|\text{AoD}| + |\text{AoA}|$ because it provided the best fit between the measurement CDFs and model CDFs. In fact, we considered other metrics as well, namely $|\text{AoD}|$, $|\text{AoA}|$, $|\text{AoD}-\text{AoA}|$, and $|\text{AoD}|+|\text{AoA}|+|\text{AoD}-\text{AoA}|$, but all rendered greater KS statistics. We also considered breaking down the angle metric into separate dimensions $|\text{AoD}|$ and $|\text{AoA}|$, but this made the corresponding 3D histograms too sparse for computation.

V. CONCLUSION

The advances in GPU-based processing over the last decade have enabled raytracing millions of facets in just seconds. This bodes well for channel modeling foliage at mmWave when precision is paramount, since the size of the leaves and branches is comparable to the signal wavelength, so their intricacies can be captured as a digital mesh with facets on the order of tens of mm^2 .

To ensure that precision translates to accuracy, in this paper the Ansys HFSS SBR+ raytracing model was applied to seven digital trees and its predictions were calibrated against measurements on counterpart live trees collected with the Terragraph 60 GHz channel sounder in summer and in winter,

TABLE 5. Comparison between measurement and model cumulative distribution functions (CDFs).



comprising a total of over half million double-directional channel scans. The calibration consisted of using electrical properties for the leaf and branches of the digital trees that correspond to 60 GHz, scaling the digital trees to the dimensions of the live trees, and trimming the leaf and branch densities. The goodness-of-fit test showed high fidelity between the measurements and the model in terms of the KS test between their CDFs.

Although the measurements were conducted in a controlled environment with a specific configuration – a specific TX power, antennas with a specific beamwidth and at a specific height, on a single tree within a subset of seven tree types, etc. – we demonstrated that when the digital foliage accurately represents the live foliage in terms of electrical properties, dimensions, and leaf and branch densities, the raytracing model can accurately predict the foliage loss of the measurements. This suggests that the raytracing will be accurate when predicting foliage loss in realistic – not controlled – environments, such as in urban, suburban, and rural environments with tens to thousands of trees or other types of vegetations like bushes and shrubs of varying dimensions, with antennas of varying beamwidths and heights, etc.

REFERENCES

- [1] *IEEE 802.11ay: Wireless LAN MAC and PHY Specifications Amendment 2: Enhanced Throughput for Operation in License-Exempt Bands Above 45 GHz*, IEEE Standard 802.11ay-2021, Jul. 2021, pp. 1–768, doi: 10.1109/IEEESTD.2021.9502046.
- [2] *Telecom Infra Project*. Accessed: 2023. [Online]. Available: <https://telecominfraproject.com/>
- [3] S. Y. Jun, C. Lai, D. Caudill, J. Wang, J. Senic, N. Varshney, and C. Gentile, “Quasi-deterministic channel propagation model for 60 GHz urban Wi-Fi access from light poles,” *IEEE Antennas Wireless Propag. Lett.*, vol. 21, no. 8, pp. 1517–1521, Aug. 2022.
- [4] D. Guven, B. F. Jamroz, J. Chuang, C. Gentile, R. D. Horansky, K. A. Remley, D. F. Williams, J. T. Quimby, A. J. Weiss, and R. Leonhardt, “Methodology for measuring the frequency dependence of multipath channels across the millimeter-wave spectrum,” *IEEE Open J. Antennas Propag.*, vol. 3, pp. 461–474, 2022.
- [5] I. A. Hemadeh, K. Satyanarayana, M. El-Hajjar, and L. Hanzo, “Millimeter-wave communications: Physical channel models, design considerations, antenna constructions, and link-budget,” *IEEE Commun. Surveys Tuts.*, vol. 20, no. 2, pp. 870–913, 2nd Quart., 2018.
- [6] H. M. Rahim, C. Y. Leow, T. A. Rahman, A. Arsad, and M. A. Malek, “Foliage attenuation measurement at millimeter wave frequencies in tropical vegetation,” in *Proc. IEEE 13th Malaysia Int. Conf. Commun. (MICC)*, Nov. 2017, pp. 241–246.
- [7] F. K. Schwing, E. J. Violette, and R. H. Espeland, “Millimeter-wave propagation in vegetation: Experiments and theory,” *IEEE Trans. Geosci. Remote Sens.*, vol. 26, no. 3, pp. 355–367, May 1988.
- [8] J. Ko, Y. S. Noh, Y. C. Kim, S. Hur, S. Yoon, D. H. Park, K. Whang, D. J. Park, and D. H. Cho, “28 GHz millimeter-wave measurements and models for signal attenuation in vegetated areas,” in *Proc. IEEE EuCAP*, Mar. 2017, pp. 1–5.
- [9] T. S. Rappaport and S. Deng, “73 GHz wideband millimeter-wave foliage and ground reflection measurements and models,” in *Proc. IEEE Int. Conf. Commun. Workshop (ICCW)*, Jun. 2015, pp. 1238–1243.
- [10] Q. Wang, X. Zhao, S. Li, M. Wang, S. Sun, and W. Hong, “Attenuation by a human body and trees as well as material penetration loss in 26 and 39 GHz millimeter wave bands,” *Int. J. Antennas Propag.*, vol. 2017, pp. 1–8, 2017.
- [11] C. U. Bas, R. Wang, S. Sangodoyin, S. Hur, K. Whang, J. Park, J. Zhang, and A. F. Molisch, “28 GHz foliage propagation channel measurements,” in *Proc. IEEE Global Commun. Conf. (GLOBECOM)*, Dec. 2018, pp. 1–6.
- [12] Y. Zhang, C. R. Anderson, N. Michelusi, D. J. Love, K. R. Baker, and J. V. Krogmeier, “Propagation modeling through foliage in a coniferous forest at 28 GHz,” *IEEE Wireless Commun. Lett.*, vol. 8, no. 3, pp. 901–904, Jun. 2019.
- [13] S. Perras and L. Bouchard, “Fading characteristics of RF signals due to foliage in frequency bands from 2 to 60 GHz,” in *Proc. 5th Int. Symp. Wireless Pers. Multimedia Commun.*, 2002, pp. 1–5.
- [14] M. Cheffena and T. Ekman, “Modeling the dynamic effects of vegetation on radiowave propagation,” in *Proc. IEEE Int. Conf. Commun.*, May 2008, pp. 1–6.
- [15] M. Celidonio, E. Fionda, M. Vaser, and E. Restuccia, “NLOS mm wave propagation measurements through vegetation in urban area: A case study,” in *Proc. AEIT Int. Annu. Conf.*, Oct. 2018, pp. 1–6.
- [16] P. Papazian and Y. Lo, “Seasonal variability of a local multi-point distribution service radio channel,” in *Proc. IEEE Radio Wireless Conf.*, Aug. 1999, pp. 1–4.
- [17] P. Zhang, B. Yang, C. Yi, H. Wang, and X. You, “Measurement-based 5G millimeter-wave propagation characterization in vegetated suburban macrocell environments,” *IEEE Trans. Antennas Propag.*, vol. 68, no. 7, pp. 5556–5567, Jul. 2020.
- [18] S. Yang, J. Zhang, and J. Zhang, “Impact of foliage on urban mmWave wireless propagation channel: A ray-tracing based analysis,” in *Proc. Int. Symp. Antennas Propag. (ISAP)*, Oct. 2019, pp. 1–3.
- [19] Y. Corre, T. Tenoux, J. Stéphan, F. Letourneux, and Y. Lostanlen, “Analysis of outdoor propagation and multi-cell coverage from ray-based simulations in sub-6 GHz and mmWave bands,” in *Proc. 10th Eur. Conf. Antennas Propag. (EuCAP)*, Apr. 2016, pp. 1–5.
- [20] P. Zhang, C. Yi, B. Yang, H. Wang, C. Oestges, and X. You, “Predictive modeling of millimeter-wave vegetation-scattering effect using hybrid physics-based and data-driven approach,” *IEEE Trans. Antennas Propag.*, vol. 70, no. 6, pp. 4056–4068, Jun. 2022.
- [21] F. A. Rodríguez-Corbo, L. Azpilicueta, M. Celaya-Echarri, P. Lopez-Iturri, A. V. Alejos, R. M. Shubair, and F. Falcone, “Deterministic and empirical approach for millimeter-wave complex outdoor smart parking solution deployments,” *Sensors*, vol. 21, no. 12, p. 4112, Jun. 2021.
- [22] R. Charbonnier, C. Lai, T. Tenoux, D. Caudill, G. Gougeon, J. Senic, C. Gentile, Y. Corre, J. Chuang, and N. Golmie, “Calibration of ray-tracing with diffuse scattering against 28-GHz directional urban channel measurements,” *IEEE Trans. Veh. Technol.*, vol. 69, no. 12, pp. 14264–14276, Dec. 2020.
- [23] J. C. da Silva and E. Costa, “A ray-tracing model for millimeter-wave radio propagation in dense-scatter outdoor environments,” *IEEE Trans. Antennas Propag.*, vol. 69, no. 12, pp. 8618–8629, Dec. 2021.
- [24] N. R. Leonor, T. R. Fernandes, M. García Sánchez, and R. F. S. Caldeirinha, “A 3-D model for millimeter-wave propagation through vegetation media using ray-tracing,” *IEEE Trans. Antennas Propag.*, vol. 67, no. 6, pp. 4313–4318, Jun. 2019.
- [25] *NVIDIA Developer*. Accessed: 2023. [Online]. Available: <https://developer.nvidia.com/rtx/ray-tracing/optix/>
- [26] D. He, B. Ai, K. Guan, L. Wang, Z. Zhong, and T. Kürner, “The design and applications of high-performance ray-tracing simulation platform for 5G and beyond wireless communications: A tutorial,” *IEEE Commun. Surveys Tuts.*, vol. 21, no. 1, pp. 10–27, 1st Quart., 2019.
- [27] H. Choi, J. Oh, J. Chung, G. C. Alexandropoulos, and J. Choi, “WiThRay: A versatile ray-tracing simulator for smart wireless environments,” *IEEE Access*, vol. 11, pp. 56822–56845, 2023.
- [28] D. He, K. Guan, D. Yan, H. Yi, Z. Zhang, X. Wang, Z. Zhong, and N. Zorba, “Physics and AI-based digital twin of multi-spectrum propagation characteristics for communication and sensing in 6G and beyond,” *IEEE J. Sel. Areas Commun.*, vol. 41, no. 11, pp. 3461–3473, Nov. 2023.
- [29] *Terragraph*. Accessed: 2023. [Online]. Available: <https://terragraph.com/>
- [30] *Ansys*. Accessed: 2023. [Online]. Available: <https://www.ansys.com/products/electronics/ansys-hfss/>
- [31] H. T. Friis, “A note on a simple transmission formula,” *Proc. IRE*, vol. 34, no. 5, pp. 254–256, May 1946.
- [32] F. Wang and K. Sarabandi, “An enhanced millimeter-wave foliage propagation model,” *IEEE Trans. Antennas Propag.*, vol. 53, no. 7, pp. 2138–2145, Jul. 2005.
- [33] F. Ulaby and M. El-Rayes, “Microwave dielectric spectrum of vegetation—Part II: Dual-dispersion model,” *IEEE Trans. Geosci. Remote Sens.*, vol. GE-25, no. 5, pp. 550–557, Sep. 1987.
- [34] D. Polder and J. H. van Santeen, “The effective permeability of mixtures of solids,” *Physica*, vol. 12, no. 5, pp. 257–271, Aug. 1946.
- [35] D. Tomasanis, “Effective dielectric constants of foliage media,” ARCON Corp., Waltham, MA, USA, Interim Report RAD-TR-90-157, Jul. 1990.
- [36] M. Jaramillo, A. W. Doerry, and C. G. Christodoulou, “Modeling tree foliage for microwave radar transparency study,” Sandia Nat. Lab. (SNL-NM), Albuquerque, NM, USA, Tech. Rep., SAND2020-14314, 2020.

- [37] F. J. Massey, "Distribution table for the deviation between two sample cumulatives," *Ann. Math. Statist.*, vol. 23, no. 3, pp. 435–441, Sep. 1952.
- [38] M. Watnik, "Advanced statistics from an elementary point of view," *J. Amer. Stat. Assoc.*, vol. 102, no. 478, pp. 766–767, Jun. 2007.



CHIEHPING LAI received the M.S. and Ph.D. degrees in electrical engineering from The Pennsylvania State University, University Park, PA, USA, in 2004 and 2007, respectively. He is currently an Electronics Engineer with the Communications Technology Laboratory, National Institute of Standards and Technology (NIST). His research interests include mmwave systems, tracking algorithms, and data processing.



DAMIR SENIC received the M.Sc. and Ph.D. degrees from the Faculty of Electrical Engineering, Mechanical Engineering and Naval Architecture, University of Split, Split, Croatia, in 2008 and 2014, respectively. From 2013 to 2014, he was a Guest Researcher with the National Institute of Standards and Technology, Boulder, CO, USA, where he worked on human exposure and wireless communications aspects of electromagnetic wave absorption in dissipative objects inside reverberant environments. From 2015 to 2018, he was Postdoctoral Research Associate with the Communications Technology Laboratory, National Institute of Standards and Technology, working on 5G measurements in highly reflective environments. He is currently the Application Engineering Manager with Ansys Inc. His research interests include millimeter wave radio communications, Over-the-Air (OTA) studies at millimeter wave and microwave frequencies, electromagnetic compatibility (EMC), and bioeffects of EM fields. In 2016, he was elected as a Distinguished Reviewer of the IEEE TRANSACTIONS ON ELECTROMAGNETIC COMPATIBILITY.



CAMILLO GENTILE (Member, IEEE) received the Ph.D. degree in electrical engineering from The Pennsylvania State University, University Park, PA, USA, in 2001. In 2021, he initiated the Radio Access and Propagation Metrology Group, Communications Technology Laboratory, and led the group, until 2023. In 2002, he joined the National Institute of Standards and Technology (NIST), in a metropolitan area. He is also leading the NextG Channel Measurement and Modeling Project. He has coauthored more than 100 peer-reviewed journals and conference papers, and two books *Geolocation Techniques* (Springer, 2012) and *Radio Propagation Measurements and Channel Modeling: Best Practices in Millimeter-Wave and Sub-Terahertz Frequencies* (Cambridge University Press, 2022). His research interests include channel modeling and physical-layer modeling for joint communications and sensing systems.



JELENA SENIC received the B.S. and M.S. degrees in electrical engineering from the University of Belgrade, Belgrade, Serbia, in 2009 and 2010, respectively. Since January 2015, she has been a Researcher with the National Institute of Standards and Technology. Her current research interests include radio propagation channel measurements and modeling at millimeter-wave frequencies. The team in which she works was a recipient of the Best Measurement Paper Award at EuCAP 2017.



NADA GOLLMIE received the Ph.D. degree in computer science from the University of Maryland, College Park, MD, USA. Since 1993, she has been a Research Engineer with the National Institute of Standards and Technology (NIST), Gaithersburg, MD, USA. From 2014 to 2022, she was the Chief of the Wireless Networks Division, NIST. She is currently a NIST Fellow with the Communications Technology Laboratory, NIST. She leads several projects related to the modeling and evaluation of future-generation wireless systems and protocols and the NextG Channel Model Alliance Chair. She is the author of *Coexistence in Wireless Networks: Challenges and System-Level Solutions in the Unlicensed Bands* (Cambridge University Press, 2006). Her research interests include media access control and protocols for wireless networks led to more than 200 technical papers presented at professional conferences, and journals, and contributed to international standard organizations and industry-led consortia.

...